8-1-2016

Identifying the Sources of Ferromagnetism in Sol-Gel Synthesized $Zn_{1-x}Co_xO$ ($0 \le x \le 0.10$) Nanoparticles

J. J. Beltrán
Universidad Popular del Cesar

C. A. Barrero
Universidad de Antioquia

A. Punnoose
Boise State University

Publication Information

Beltrán, J.J.; Barrero, C.A.; and Punnoose, A. (2016). "Identifying the Sources of Ferromagnetism in Sol-Gel Synthesized $Zn_{1-x}Co_xO$ ($0 \le x \le 0.10$) Nanoparticles". *Journal of Solid State Chemistry, 240*, 30-42. http://dx.doi.org/10.1016/j.jssc.2016.05.013

Identifying the Sources of Ferromagnetism in Sol-Gel Synthesized $Zn_{1-x}Co_xO$ ($0 \leq x \leq 0.10$) Nanoparticles

J.J. Beltrán[1, 2], C. A. Barrero[1] and A. Punnoose[2]

[1]*Grupo de Estado Sólido, Facultad de Ciencias Exactas y Naturales, Universidad de Antioquia UdeA, Calle 70 No 52-21, Medellín, Colombia.*

[2] *Department of Physics, Boise State University, Boise, Idaho 83725-1570, USA.*

ABSTRACT

We have carefully investigated the structural, optical and electronic properties and related them with the magnetism of sol-gel synthesized $Zn_{1-x}Co_xO$ ($0 \leq x \leq 0.10$) nanoparticles. Samples with $x \leq 0.05$ were pure and free of spurious phases, whereas $ZnCo_2O_4$ was identified as the impurity phase for samples with $x \geq 0.08$. Samples with $x < 0.05$ were found to be true solid solutions with only high spin Co^{2+} ions into ZnO structure, whereas sample with $x = 0.05$, exhibited the presence of high spin Co^{2+} and low spin Co^{3+}. For the impurity-free samples we found that as Co concentration increases, *a* and *c* lattice parameters and Zn–O bond length parallel to the *c*-axis decrease, the band gap drastically decreases, and the average grain size and distortion degree increases. In all samples there are isolated Co^{2+} ions that do not interact magnetically at room temperature, bringing about the observed paramagnetic signal, which increases with increasing Co concentration. *M* vs *T* curves suggest that some of these disordered Co^{2+} ions in $Zn_{1-x}Co_xO$ are antiferromagnetically coupled. Moreover, we also found that the intensity of the main EPR peak associated to Co^{2+} varies with the nominal Co content in a similar manner as the saturation magnetizations and coercive fields do. These results point out that the ferromagnetism in these samples should directly be correlated with the presence of Co^{2+}. Bound magnetic polaron model is insufficient to explain the Room temperature ferromagnetism in these Co doped ZnO samples and the charge transfer model seems not influence considerably the FM properties of $Zn_{1-x}Co_xO$ nanoparticles. The FM behavior may be originated from a combination of several factors such as the interaction of high spin Co^{2+} ions, the formation of defect levels close to the valence band edge and grain boundaries effects.

Keywords: Co doped ZnO nanoparticles; Optical Absorption; EPR, XPS, Room temperature ferromagnetism. * *Corresponding Author E-mail: jjbj08@gmail.com*

1. INTRODUCTION

ZnO is a semiconducting material, which has a direct wide-band gap (E_g~ 3.3 eV) at room temperature (RT) with a large exciton binding energy of 60 meV.[1] ZnO is attracting attention because of its multiple applications such as light-emitting diode, transparent conductor oxide, varistor, surface acoustic wave device, piezoelectric transducer, chemical gas sensor, biosensor and as window material for display and solar cells. [2] It is well known that the electrical and optical properties of ZnO can be tuned by modifying its electronic structure via extrinsic doping with selective elements. Transition metal (TM) doping in ZnO nanostructures has been proposed to develop dilute magnetic semiconductor (DMS) which will make them attractive for new nanoelectronic and spintronics applications.[3] These DMS materials have attracted much attention as promising functional materials because of the possibility of manipulating, in a controllable way, charge and spin degree of freedom of free carriers in a single substance.[4] These materials must exhibit an intrinsic ferromagnetism at RT or above arising from the doped matrix. To satisfy such system, the foreign atoms should be distributed the most homogeneous manner as possible in the crystalline structure of the host semiconductor. The role of Co ions on the magnetism in this TM doped ZnO system has been widely explored both theoretically and experimentally with poor agreement in the reported results. In relation with the theoretical studies Lee and Cheng[5] found that the spontaneous magnetization is not possible in intrinsic Co doped ZnO, that the ferromagnetic (FM) coupling is short ranged and that a high concentration of both Co ions and electron carriers are needed to achieve

ferromagnetism. On the other hand, the theoretical studies by Spaldin[6] and Gopal and Spaldin[7] resulted in that the energy difference between the antiferromagnetic (AFM) and FM couplings was very small. Therefore paramagnetic (PM) behavior was predicted in the absence of free carriers, but when holes were introduced by creating Zn vacancies, the FM state was then stabilized. The influence of Co concentration on the magnetic interactions is also not clear. While some groups reported room temperature ferromagnetism for 25 at.% and lower concentrations (≤ 15 at.%) of Co, other groups reported the absence of FM behavior.[3] Now, regarding the experimental investigations, Kittilstved and Gamelin[8] and Schwartz *et al*[9] have studied Co^{2+} doped ZnO thin films and evidenced chemical activation of long-range FM coupling mediated by shallow donor electrons. Lawes *et al.*[10] reported absence of ferromagnetism, but dominant AFM interaction, down to 2 K in bulk $Zn_{1-x}Co_xO$ with $0.02 \leq x \leq 0.15$. Mesaros *et al*.[11] prepared $Zn_{1-x}Co_xO$ (x = 0.05, 0.10, and 0.15) nanoparticles using a wet-chemical synthesis route, and from their temperature dependence of the EPR integral intensity, a FM behavior was revealed for the samples. However, a possible origin for this magnetic interaction was not provided. Fu *et al.*[12] prepared Co doped ZnO nanomaterials by using a hydrothermal method, and discussed that the observed ferromagnetism originates probably from the Co^{3+} enrichment and the coexistence of Co^{2+}/Co^{3+}on the particle surface, which may lead to the super-exchange or a double-exchange mechanism between those ions. Gandhi *et al.*[13] synthesized by a co-precipitation method Co doped ZnO nanoparticles and reported that the donor defects, such as oxygen vacancies and zinc interstitials, were found to be the main reasons for the observed room temperature ferromagnetism (RTFM). On the other hand, Acosta-Humánez *et al.*[14] studied using EPR some Co doped ZnO nanoparticles prepared by a sol-gel

method. The authors reported that the ferromagnetism of the materials is governed by FM coupling among cobalt ions, but a possible microscopic mechanism is not offered. Now, Hays *et al.*[15] studied sol gel-synthesized $Zn_{1-x}Co_xO$ ($0 \leq x \leq 0.12$) nanoparticles, and found a PM behavior with increasing AFM interactions as x increased to 0.10. They also reported a weak FM behavior for the sample with $x = 0.12$, and proposed that this high Co concentration and appropriate oxygen stoichiometry may be needed to achieve adequate FM interaction between the Co^{2+} ions. Kumar *et al.*[16] investigated sol-gel synthesized $Zn_{1-x}Co_xO$ ($0 \leq x \leq 0.04$) nanoparticles and reported RTFM in the samples which increases with increasing Co concentration. They suggested that the joint effects of the intrinsic exchange interactions arising from oxygen vacancy assisted bound magnetic polarons and the grain boundary effects were responsible for the RTFM in this system. Tahir *et al.*[17] prepared Co doped ZnO nanorods and found that surface defects such as oxygen vacancies are likely a source of RTFM. They mentioned that oxygen vacancies are likely to congregate at low-energy (101) and (100) surfaces, instead of inside the bulk.

Clearly, from this short controversial literature review, it is noticed that more investigations are still required. In this paper, we carefully characterize the crystallographic, vibrational, optical and magnetic properties of $Zn_{1-x}Co_xO$ ($0 \leq x \leq 0.10$) nanoparticles prepared by a sol-gel method. The main goals are to: (i**)** provide information about the solubility limit of Co dopant ions in ZnO lattice, (ii) search for the oxidation and spin states of Co ions, (iii) discern the participation of Co in the RTFM signal, (iv) infer about the preferred location of the Co (Co^{2+} and/or Co^{3+}) ions in the ZnO lattice, and (v) to contribute to the understanding of the role of cobalt ions on the magnetic properties of Co doped ZnO.

2. EXPERIMENTAL DETAILS

$Zn_{1-x}Co_xO$ ($0.0 \leq x \leq 0.10$) nanopowders were prepared by the citrate precursor method based on the modified Pechini process.[18] Required amounts of $Zn(NO_3)_2 \cdot 6H_2O$, $Co(NO_3)_2 \cdot 6H_2O$, citric acid (CA), ethylene glycol (EG), ammonia solution and deionized water were used for the preparation of the starting sol. The black powder precursors resultants after the polyesterification reaction were annealed in a tubular furnace at 550 °C (heating rate: 5 °C/min) in air atmosphere for 1 and 3 h. To obtain insight into possible Co impurity phases which might be formed under these synthesis conditions, Co_3O_4 was also prepared following identical synthesis procedures. These fine powders of the as-obtained products were characterized by X-ray diffraction (XRD), fourier transform infrared spectroscopy (FTIR), optical absorption measurements, X-ray photoelectron spectroscopy (XPS), electron paramagnetic resonance (EPR) and variable temperature magnetic measurements. Detailed experimental section and characterization studies were carried out following procedures as described previously in references [19] and [20].

3. RESULTS

3.1 *X-ray Diffraction*: Figure 1 presents the XRD refined patterns of $Zn_{1-x}Co_xO$ samples annealed for 1 h along with that of Co_3O_4 sample prepared as reference. The hexagonal würtzite ZnO crystal structure was discerned as the only phase in the $Zn_{1-x}Co_xO$ nanopowders with x in the range of $0.0 \leq x \leq 0.05$, without the appearance of any extra peak. However, additional weak peaks located at 59.3^o and 65.1^o were observed in the XRD patterns with higher Co content ($x \geq 0.08$). These peaks were more clearly noticed when the y-axis is plotted in logarithmic scale and matched well either with diffraction (511) and

(440) planes of Co_3O_4 and/or $ZnCo_2O_4$. Although, it is difficult to distinguish between Co_3O_4 and $ZnCo_2O_4$ using XRD due to their equivalent spinel structures with nearly identical lattice constants (a= 8.088 Å), Co_3O_4 has been reported as the primary foreign phase in Co doped ZnO system.[11], [21]–[23] In view of this, we have fitted these XRD patterns assuming cobalt oxide as the secondary phase, with positional occupancies of (x, y, z) for Co-1 at (0.1250, 0.1250, 0.1250), Co-2 at (0.500, 0.5000, 0.500) and O at (0.2631, 0.2631, 0.2631), but good results were not obtained. Then, we performed a second attempt including $ZnCo_2O_4$ phase, with positional occupancies of (x, y, z) for Zn at (0, 0, 0), Co at (0.625, 0.625, 0.625) and O at (0.3881, 0.3881, 0.3881), improving statically the fitting (χ^2 and Bragg R- factor for secondary phase). The result is that this phase accounts for 0.5 and 0.9 wt. % in the XRD patterns of x= 0.08 and 0.1 samples, respectively (indicated by orange vertical bars in the fit). From the magnified regions of the XRD patterns, showed in top panel at the right side of the Figure 1, can be noted that for $x \leq 0.05$, with increasing Co concentration, the XRD peak positions of Co doped ZnO samples are shifted towards higher diffraction angles and then for $x > 0.05$ are shifted to lower angles with further rise in the doping. The lattice parameters for all samples, annealed for 1 h, are displayed in left part of Figure 2. The a and c lattice parameters of ZnO as well as the cell volume gradually decrease with the increase in doping concentration and tend to have a minimum at doping level of 5 % and then increase with further rise in the doping [see panel (a) in left part of Figure 2], while parameter L[24] (Zn–O bond length along the c direction) follows the same trend [see panel (b) in left part of Figure 2)]. Interestingly, the average crystallite size (Dv) increases with the increase of Co concentration [see panel (b) in left part of Figure 2]. This result suggests that Co ions in ZnO structure could encourage crystallite growth,

speeding up further growth of ZnO grains. Similar changes have been observed by other authors.[16], [25]It can be seen from panel (c) in left part of Figure 2 that the *R* parameter [26] increases and the *c*/*a* ratio decreases as *x* increases to 0.05, and above this nominal percentage a definite trend is not observed, which could be related with the formation of $ZnCo_2O_4$ phase on further doping of Co above 5 %. In a tetrahedral environment and high spin state, the ionic radii of Co^{2+} and Zn^{2+} are 0.58 and 0.60 Å, respectively. Then, it is expected that the lattice parameters tend to decrease slightly with increasing Co concentration for a solid solution $Zn_{1-x}Co_xO$ as observed here (maximum $\Delta a/a$ and$\Delta c/c$ of $9*10^{-4}$ and $2*10^{-3}$ respectively). Thus, the lattice parameters calculated from the XRD data indicate that the solubility limit of Co ions in the ZnO wurzite structure is lower than 8 at. % doping, indicating that at least 5% of the Zn^{2+} sites in ZnO lattice can be replaced successfully by the Co ions. On further Co doping above $x = 0.05$, segregation of, more probably, $ZnCo_2O_4$ occurs.

On the other hand, XRD patterns of Co doped ZnO nanoparticles annealed for 3 h (data not shown) displayed similar diffractions peaks as those observed for the samples annealed for 1 h, but in this case, besides the peaks located at 59.3^o and 65.1^o, two additional peaks located at ~36.8 ^{o} and ~44.4 ^{o} were observed in the XRD patterns of the 8 and 10 at. % of Co doped samples, when the *y*-axis was plotted in logarithmic scale. The fitting improved considerably by including the $ZnCo_2O_4$ phase instead of Co_3O_4, corroborating again the former compound as the spurious phase in these two set of samples. The fitting showed similar *a* and *c* lattice parameters and slightly higher *Dv* values in comparison to these for samples annealed for 1 h as shown in the right part of Figure 2. Additionally, from this

Figure, it can be inferred that in this set of samples the solubility limit of Co ions in the ZnO wurzite structure is also lower than 8 % doping.

It is worth mentioning that the Williamson-Hall plot [27] did not show linearity neither in undoped nor in Co doped ZnO samples by contrast, scattered points were observed, which could indicate that this preparation method gives rise to non-homogeneous particle shape and size distributions.

3.2 ***Fourier transformed infrared spectroscopy***: Figure 3 shows the FTIR spectra in the wavenumber range of 400-4000 cm^{-1} for $Zn_{1-x}Co_xO$ with x = 0, 0.01, 0.03 and 0.05 annealed for 1 h. The intense band centered at around 450 cm^{-1} is assigned to antisymmetric stretching vibration of O-Zn-O bonds, which also confirms the wurtzite structure.[28] All spectra exhibit two very weak peaks located at ~2850 and 2925 cm^{-1} due to C-H bond bending and stretching, respectively and two weak bands at 1390 and 1630 cm^{-1} attributed to the antisymmetric and symmetric C=O stretching modes, commonly associated with the carboxylate functional group, possibly originating from the fragments of the citrate precursor. It is worth mentioning that these bands are not considered as contaminations of the nanoparticles, rather they point out to the presence of absorbed species on the surface of nanopowders that could influence the properties of ZnO that depends primarily on the surface structure.[29] The intense and broad absorption in the range of 3100-3700 cm^{-1} is due to the stretching vibration of hydroxyl groups attached on the surface of nanocrystalline powders, indicating the existence of water absorbed on the surface of ZnO grains. This possibly could be attributed to the polarity of ZnO. Water dissociation often is favored at ZnO oxide surfaces, leaving OH^- groups and hydrogen ions (H^+) ions, where the stacking of

Zn^{2+} ($000\bar{1}$) plane ions tends to bind the hydroxide and the stacking of O^{2-} (0001) plane ions tends to under-coordinated with the hydrogen, due to the electrostatically instability of these planes.[30] From Figure 3, it can be observed that the intensity of OH^-, C-H and C=O stretching modes, with respect to Zn-O bands, decrease with Co doping. OH^-group is considered a potential *n*-type defect in ZnO. Then, these results could suggest that intrinsic *n*-type defects may be suppressed with increment of Co content. Additionally is observed that with increasing Co content from x = 0.01 to 0.03 the intensity ratio of OH- to Zn-O stretching modes increases and then decreases when x reaches 0.05.

3.3 *Optical absorption*: Optical absorption spectroscopy is considered a versatile tool to reveal electronic transitions when Co^{2+} ions are incorporated into ZnO lattice substituting Zn^{2+} at tetrahedral sites of the ZnO wurtzite structure and for studying the effect of Co doping concentration on the band gap of ZnO. RT optical absorption spectra of undoped and Co doped ZnO nanopowders, annealed for 1 h at different Co concentrations as well as Co_3O_4 sample prepared under the same conditions are shown in Figure 4 (a). The introduction of Co ions into ZnO lattice lead clearly to the appearance of three well defined additional absorption peaks as compared with the spectrum of undoped ZnO. These peaks located around 567, 610 and 655 nm are related to d-d transitions of Co^{2+} involving crystal field levels in a tetrahedral crystal symmetry and can be ascribed to the (F) $\rightarrow$ $^2E(G)$, $^4A_2(F) \rightarrow {}^4T_1(P)$, and $^4A_2(F) \rightarrow {}^2A_1(G)$ transitions, respectively, where A, E and T are generally designations of intermediate energy bands.[17], [31], [32] These results support the fact that high spin tetrahedrally coordinated ($3d^7$, S=3/2) Co^{2+} ions are substituting at the Zn^{2+} sites in the ZnO structure. From this Figure 4 (a) it is evident that the relative

intensity of the absorption bands (area under curve) between 525 and 725 nm do increase with increasing Co concentration, indicating higher absorption by the Co^{2+} ions incorporated in ZnO. To probe further into the details of differences among the samples, we have differentiated the absorbance with respect to the wavelength and the results are depicted in Figure 4 (b). Besides the strong absorption peak centered at ~380 nm, which arises from ZnO at the band edge, and the peaks related to d-d transitions of Co^{2+} ions, there are two additional humps located at ~420 nm and ~510 nm in Co doped ZnO samples, this latter is evident in $Zn_{1-x}Co_xO$ samples with $x \geq 0.05$. As x increases from 0 to 0.05, the peak at 380 nm sharply decreases and suddenly disappears at $x = 0.03$. On the other hand, the relative intensity of the peak located at 420 nm increases and is shifted to higher wavelengths with increasing x up to $x = 0.05$ and then it remains almost constant onwards. Regarding to the broad peak located at ~510 nm, this does not change the position with increasing Co^{2+} ions, but weakly increases its intensity. Let us now briefly discuss the origin of these two additional humps. Patra *et.al* [33] have proposed that the band located at 425 nm in the spectrum of Co doped ZnO can be assigned to the presence of Co^{3+} ions tetrahedrally coordinated with oxygen corresponding to 5E to $^5T_2$ transition. However, this interpretation should be taken with care because according to XPS and EPR results (presented below) the presence of Co^{3+} is only detected in $Zn_{1-x}Co_xO$ samples when x reaches 0.05. On the other hand, Schwartz *et. al* [9] in Co doped ZnO nanocrystals have observed a band close to the absorption band edge which has been related as one of the spin-forbidden Co^{2+} ligand-field charge transfer (CT). Similar observations were found by Shi *et. al* in Co doped ZnO nanorods. [23] Therefore, the broad peak located at 425 nm has been commonly assigned to sub-band gap ligand to metal charge-transfer (LMCT) in which the Co^{2+} acts as the CT acceptor and the valence band serves as the CT donor. Thus, Co^{2+}

rich zone below band gap can promote ligand field CT and semiconductor band-to-band transitions. Now, the shoulder at 510 nm has been assigned to the $^4T_{1g}(F) \rightarrow 4T_{1g}(P)$ and $4T_{1g}(F) \rightarrow 4A_{2g}$ ligand-field transitions of pseudo-octahedral Co^{2+} ions.[9], [21] Taking into account XPS, EPR and XRD results, these pseudo-octahedral Co^{2+} ions, present in x = 0.01 and 0.03, could be more easily converted into pseudo-octahedral Co^{3+} ions when x reaches 0.05 and with further increment of Co doping, the additional broadening of 510 nm peak could indicate the formation of the spinel structure of $ZnCo_2O_4$ as secondary phase**.** The inset in Figure 4 (a) shows the band gap (*Eg*) variation, obtained following the Kubelka-Munk rule [34] as a function of nominal Co content (red solid spheres). The Co_3O_4 sample gave two *Eg* values, 1.61 and 2.22 eV, similar to those reported in the literature and which are lower than the *Eg* observed in all the Co doped ZnO samples.[35] From inset of Figure 4(a) it can be seen that the band gap decreases with increasing Co concentration, indicating the red shift of the band gap as observed by Elilarassi and Chandrasekaran [31] and Hays *et.al* [15] Our results are also in close agreement to those reported by Qiu *et.al* [36] They have observed that the decrease of the band gap in $Zn_{1-x}Co_xO$ nanonorods with $0 \leq x \leq 0.1$ follows the relationship $\Delta E_g = 0.54(e^{-x/0.03} - 1)$ eV where x is Co^{2+} concentration. As shown by the blue solid triangles in the inset of Figure 4 (a), the decrease in the band gap with the increase in Co concentration follows well this trend. The abnormal narrow band gap energies found by Qiu *et.al* [36] were indicated to originate from *s,p-d* exchange interactions that are proportional to the square of lattice volume. In this work we have not observed a direct correlation between E_g and the variation of the lattice parameters or cell volumes in Co doped ZnO samples. Then, this gradual decrease in the band gap for $Zn_{1-x}Co_xO$ samples, with the increase of x may be mainly related to the

stronger exchange interactions between the localized *d* electrons of the Co ions substituting for Zn^{2+} ions and the *s* and *p* electrons of the host band of ZnO.[37], [38] The strong *s,p–d* hybridization ion probably lowers the bottom of the conduction band, while heightening the top of the valence band resulting in a band gap narrowing.

Optical absorption spectra and derivative absorbance of $Zn_{1-x}Co_xO$ ($0 \leq x \leq 0.1$) nanoparticles annealed for 3 h showed similar results as those found for the samples annealed for 1 h [(see Figures 5 (a) and 5 (b)], except that the broad peak located at ~510 nm is more evident at $x = 0.03$. In comparison to the samples annealed for 1 h, those annealed for 3 h exhibited slightly smaller band gaps of 3.22, 3.04, 2.86, 2.77, 2.69 and 2.6 eV for $x = 0$, 0.01, 0.03, 0.05, 0.08, and 0.10, respectively, and follows the same trend in the relationship $\Delta E_g = 0.54(e^{-x/0.03} - 1)$, except for the last doping concentration. It is worth mentioning that the areas under the curves of the absorption bands between 525 and 725 nm in Figure 5 (a) increase as *x* increases to 0.05 and then decrease with further rise in the doping, indicating higher Co^{3+} content for $x \geq 0.08$ in these samples annealed for 3 h.

As mentioned above, these band gap values are smaller than those for the samples annealed for 1 h, although the latter samples have smaller crystallite sizes compared to the former ones (3 h annealed samples). These results can be due to the fact that the structural changes, caused by the dopant incorporation and the prolonged annealing time, have a dominant role in the observed changes of the band gaps.

3.4 ***X-Ray Photoelectron Spectroscopy*****:** Figure 6 (a) shows full wide-scan X-ray photoelectron spectra of $Zn_{1-x}Co_xO$ with x = 0, 0.01, 0.03, and 0.05 annealed for 1 h. All of the peaks in undoped ZnO can be only ascribed to Zn, O, and C along with their auger peaks and no magnetic impurity within the detection limit was observed, meanwhile in Co doped ZnO nanoparticles, additionally to these peaks, Co element was clearly evidenced as labeled in the Figure. The Zn $2p_{3/2}$ core level data of $Zn_{1-x}Co_xO$ samples with $0.01 \leq x \leq 0.05$ are displayed in Figure 6 (b). All the spectra were deconvoluted using a single and symmetric signal located around 1021.3 eV and no significant changes in the chemical shift in comparison to undoped ZnO sample were observed [(see the inset in Figure 6 (b)]. The slight change in the binding energies (BE) of Zn $2p_{3/2}$ peak for these samples compared to that of bulk ZnO (1021.8 eV) [39] may be due to the nanometric size of these powders. The observed BE values indicates that Zn atoms retain the bivalent state in tetrahedral sites surrounded by O^{2-} ions. The intensity and relative area under the Zn $2p_{3/2}$ peak progressively decreases upon increasing the Co doping, confirming that the Co^{2+} ions incorporate at the Zn^{2+} site. From the survey spectra similar results were observed when the relative areas under Zn $L_3M_{4,5}M_{4,5}$ (490-505 eV) Auger peak and 3*p* core region were plotted against x. Figure 6 (c) shows the high-resolution XPS of O 1*s* core level spectra of $Zn_{1-x}Co_xO$ samples with x = 0.01, 0.03 and 0.05 along with that of Co_3O_4 sample. The broad and asymmetric shape of this signal was deconvoluted into two components indicating the presence of two different oxygen bonded species. The first peak with lower BE centered at ~530.2 eV (O 1*s*-1) is attributed to O^{2-} ions in the hexagonal wurzite ZnO structure which are bonded to Zn^{2+} and substitutional Co^{2+} atoms in tetrahedral sites, located mainly in the core region. The second BE peak (531.2-531.5 eV, O 1*s*-2) can be

associated to weakly bound –O*H* bonds located at the surface of ZnO nanoparticles, as observed by FTIR. Changes in this latter component may be related to changes in the concentration of oxygen vacancies and/or defects on the surface of ZnO nanoparticles and/or oxygen-deficient regions within the matrix of ZnO.[40]–[42] It is worth mentioning that Co doped ZnO samples did not show chemical shift in the BE in comparison to undoped ZnO sample. With increasing Co doping concentration from x = 0.01 to 0.03, the intensity of the O 1*s*-1peak decreases, and then increases when x reaches 0.05. On the other hand the FWHM of O 1*s*-2 peak slightly increases, but its relative area slightly decrease from x = 0.01 to 0.05. It is worth mentioning that the ratio of the areas of the O 1*s*-1to the O1*s*-2 peaks decreases with increasing x from 0 to 0.03 and then increases for x=0.05. These observations could probably suggest that exists a maximum of oxygen deficient regions within the ZnO matrix at x = 0.03. These results may also indicate that the distribution of oxygen vacancies and defects on the surface of Co doped ZnO nanoparticles do not vary significantly as Co content increases. Regarding the reference sample, the O1*s*-1 peak in Co_3O_4 at 529.5 eV, can be assigned to oxygen ions in their respective lattice sites, while the peak located at 532.5 eV (O 1*s*-3) in Co_3O_4 may be due to -CO_3 surface contamination.[43] From these results and as is observed in Figure 6 (c), it is clear that the presence of O1*s*-1 and O1*s*-2 peaks in the Co doped ZnO samples highlight the difference in the chemical environment of the oxygen ions.

Figure 6 (d) shows high resolution XPS scans of the Co 2*p* core electron regions of the $Zn_{1-x}Co_xO$ ($0.01 \leq x \leq 0.05$) samples annealed for 1 h and also the spectrum of Co_3O_4, which is included as reference. The Co 2*p* core-electron spectra of $Zn_{1-x}Co_xO$ with x = 0.01 and 0.03

were deconvoluted into two components. The first component lies in the range of 780.9-781.0 eV with ΔS of 15.6-15.8 eV, whereas the second component that appears at 786.0-786.2 eV is associated with shake-up satellite peaks (SS). Note that the spin-orbit splitting (ΔS) values of these Co ions are much higher than those for metallic Co (15.1 eV) or CoO (15.2 eV), but they are close to $Co(OH)_2$ (15.9 eV)[44] and to Co_3O_4 (15.8 eV for Co^{2+} component). This observation, along with the presence of the strong SS around 5.2 eV of the 2*p* core level confirms that the valence state of Co ions in the ZnO structures are mainly 2+ and of high spin and that they are substituting Zn^{2+} at the tetrahedral site surrounded by O^{2-} ions.[45] On the other hand, in the spectrum of $Zn_{0.95}Co_{0.05}O$ sample, the introduction of two additional components was necessary to improve considerably the deconvolution. These two new components with main line of 779.7 eV and ΔS of 15.2 eV and the small SS located at 790.1 eV can be associated to Co^{3+} ions.[46] Although, small differences in the BE and ΔS values for Co^{3+} component in $Zn_{0.95}Co_{0.05}O$ in comparison to those for the reference sample (779.3eV and ΔS of 15.1 eV) were observed, the XPS technique is insufficient to differentiate between Co^{3+} ions in wurzite structure and Co^{3+} in Co_3O_4 or $ZnCo_2O_4$, due to the overlapping of these Co^{3+}components in XPS spectra. From Figure 6 (d) can be seen that the strong SS of the 2*p* core level increase with *x* from 0.03 to 0.05, which imply that the electronic state of Co^{2+} ions is largely in high spin arrangement, resembling that of CoO rather than that of Co_3O_4 or $ZnCo_2O_4$, which can also be deduced from the lack of SS in the latter compounds. In order to confirm if any secondary phase is present in the $Zn_{0.95}Co_{0.05}O$ sample, we have recorded XRD patterns with extended accumulation time enhancing the detection limit considerably (data not shown). This pattern did not reveal any phase other than ZnO, even when plotted in logarithmic scale. Additionally, careful analysis of the spectra for $Zn_{1-x}Co_xO$ ($0.01 < x < 0.05$) did not show

any noticeable change in the peak positions of Zn 2*p* and O 1*s* core level upon increasing the Co content, ruling out the presence of any impurity phase[19]. According to the Shannon ionic radii Table, Co^{3+} exists in octahedral environments and not in tetrahedral ones, then, it is possible to assume that these Co^{3+} ions probably are occupying interstitial and/or superficial (where the presence of oxygen vacancies and/or defects is higher) sites in ZnO grains, instead of forming any secondary phase. It is noted that relative area under O1-*s*2 peak remains almost unchanged with increasing Co doping and that oxygen deficient region within the ZnO matrix decreases in $Zn_{0.95}Co_{0.05}O$ sample. On the other hand, the BE of Co^{3+} component in $Zn_{0.95}Co_{0.05}O$ sample is slightly higher than that of Co_3O_4, suggesting that Co^{3+} ions in wurzite structure have slightly lower symmetry and additionally exists small difference in ΔS of the $Zn_{0.95}Co_{0.05}O$ and Co_3O_4 samples (for Co^{3+} component), suggesting that Co^{3+}ions could be presumably located in both surface and core-interstitial region, occupying distorted octahedral sites i.e., pseudo-octahedral environment.

3.5 ***Electron Paramagnetic Resonance*****:** Figure 7 illustrates the experimental EPR spectra recorded at a chosen temperature of 5 K for $Zn_{1-x}Co_xO$ with $0.01 \leq x \leq 0.10$ annealed for 1 h. In these types of compounds, the cobalt atoms substitute the zinc atoms and the neutral charge state is commonly Co^{2+} ($3d^7$ configuration). ^{59}Co has I=7/2 which gives rise, in single crystals, to an eight line hyperfine pattern, when the magnetic field is along the *c*-axis.[11], [47] The spectra are composed of a dominant sharp peak centered at around 1526 G ($g_x = g_y = 4.6$) and a weaker and relatively broad signal at 3015 G ($g_z = 2.2$). These lines are attributed to the perpendicular component ($H \perp c$) corresponding to tetrahedrally coordinated paramagnetic (PM) Co^{2+} ions substituting at Zn^{2+} sites in the wurzite ZnO

structure and to the parallel component *(H || c)* respectively, suggesting that the system symmetry is axially distorted.[11] The lines with a *g* value of ~1.96 or 2.004 associated to shallow donors or core-shell vacancies originating from zinc and oxygen vacancies respectively [48], [49] and the EPR line at 2800 G, probably attributed to the Co_3O_4, were not detected.[11] It is worth mentioning that seven hyperfine components (average hyperfine coupling constant A ~ 200 G), around the signal located at 3015 G, marked by arrows in the inset (a) of Figure 7, can be observed in the spectrum of $Zn_{0.99}Co_{0.01}O$ sample. As Co doping concentration increases, the hyperfine splitting disappears due to increased interaction between the doped Co^{2+} ions. From Figure 7, it can be seen that the 1500 G signal became increasingly broadened (from 130 to 450 G) with increasing Co concentration. This behavior is correlated to the large concentration of spins of the isolated Co^{2+} ions, which is known to contribute to the broadening of the signal. It is well known that the EPR spectra of the Co dopant in the ZnO nanopowders depend strongly on the Co concentration and that the area under the integrated spectrum is proportional to the spin concentration. In order to investigate this variation, the EPR spectra have been performed keeping all controllable experimental parameters constant such as microwave power, frequency, field modulation and sample mass. Inset (b) of Figure 7 shows the double integration of the corresponding experimental EPR spectra plotted as a function of *x*. It is noted that initially the EPR signal intensity increases from $x = 0.01$ to $x = 0.03$, reaching a maximum at this concentration and then decreases as *x* increases. These results, along with the XPS data discussed above, strongly point out that a significant fraction of the interacting high spin Co^{2+} (S=3/2) ions are converted into low spin Co^{3+}(S=0) state as *x* increases from 0.03 to 0.05. According to EPR, XRD, XPS and optical absorption results,

these observations may suggest that there is a mixture of valence ions, Co^{3+} and Co^{2+}, at x = 0.05 and beyond this concentration some of these Co^{3+} ions can be segregated as $ZnCo_2O_4$. Summarizing, XRD, optical absorption, XPS and EPR results suggest that there exist a solid solubility limit of Co^{2+} ions in Co doped ZnO when $x \leq 0.03$, and some of these Co^{2+} are converted into Co^{3+}, when x = 0.05. Upon further Co doping above 0.05, the Co^{3+} ions concentration must exceed the absolute solid solubility limit. Then, Co^{3+} atoms cannot be solid dissolved into the ZnO lattice, so that they form an impurity phase containing Co^{3+} ions such as $ZnCo_2O_4$.

3.6 ***Magnetic Measurements*****:** Figure 8 shows the 5K and RT M vs H curves of all Co doped ZnO samples along with Co_3O_4 annealed at 550 ^oC for 1 h. Hysteresis loops at 5K of all samples including Co_3O_4, showed a linear behavior (see the insets of Figure 8). At RT, it can be seen that with increasing Co concentration, the linear part, owing to the PM component, increases [(see also Figure 11 (b)]. This result is in full agreement with EPR data, indicating large concentration of isolated Co^{2+} ions as x increases. Clear hysteresis loops are observed in the samples with $x \leq 0.03$ suggesting the presence of FM interaction at RT. The openings of these M vs H curves decreases substantially with further rise in the doping, indicating a paramagnetic and/or superparamagnetic-like behavior from x = 0.05 onwards. Figure 9 depicts the RT M vs H curves of $Zn_{1-x}Co_xO$ ($0 \leq x \leq 0.08$) samples, where the linear component has been subtracted (M-$\chi_p$vs H), to illustrate the actual M_s and H_c expected for a FM phase. Here, it is worth mentioning that undoped pure ZnO exhibits very weak RT ferromagnetism (RTFM) with saturation magnetization (M_s) of about 0.47 memu/g.[11] Now, clear FM behavior was observed for $Zn_{1-x}Co_xO$ samples with x = 0.01 and 0.03, while it markedly decreased for x = 0.05. On the other hand, $Zn_{0.92}Co_{0.08}O$ sample

showed a closed and somewhat strange *M* vs *H* curve, possibly indicating the presence of an impurity magnetic phase in addition to the dominant Co doped ZnO. The $Zn_{0.90}Co_{0.10}O$ sample was lacking of hysteresis loops evidencing a superparamagnetic (SP) like behavior (see lower inset of Figure 9), with higher *Ms,* indicating the existence of other magnetic interactions due to the presence of a dominant secondary phase. The variation of M_s and H_c as a function of nominal Co content for $Zn_{1-x}Co_xO$ ($0 \leq x \leq 0.08$) samples are plotted in upper inset of Figure 9. Both M_s and H_c parameters increases reaching maximum values for $x = 0.03$ and then decreases as x increases further. Interestingly, the variations of M_s and H_c show similar trend as the intensity of the EPR signal at 5K. The low M_s values and the presence of the PM component observed in these samples suggest that only a small fraction of the doped Co^{2+} ions participate in the ferromagnetically coupled state, which results in weak ferromagnetism.

Figure 10 shows the temperature dependence of the magnetization for Co doped ZnO samples annealed for 1 h along with that for Co_3O_4 sample in both ZFC and FC conditions for the applied field value of $H = 500$ Oe from 5 to 300 K. The *M* vs *T* curves of $Zn_{1-x}Co_xO$ samples present a concave nature similar to PM materials. On the other hand, ZFC and FC curves of Co_3O_4 sample exhibit a Neel temperature of 35 K indicating its AFM behavior. These curves were fitted following the modified Curie-Weiss law, $\chi = \chi_o + C/(T+\theta)$, where χ_o represents non-paramagnetic contributions, $C = Nu^2/3K_B$ (N is the number of magnetic ions/g, u is the magnetic moment of the ion, K_B is the Boltzmann constant) and θ is the Curie-Weiss temperature. The values of C and θ [(see Figure 11 (a)] indicate that the interaction between the disordered paramagnetic-like Co^{2+} spins (χ_p) [(see Figure 11(b)], observed in the RT *M* versus *H* data are AFM in nature.

In Figure 11 (b) it can be seen that χ_o increases from $x = 0.01$ to 0.03 and slightly decreases for $x = 0.05$ and then increases again with further doping. The large increase of χ_o in the $Zn_{1-x}Co_xO$ samples with $x \geq 0.08$ can be due to the presence of $ZnCo_2O_4$. The decrease of χ_o for $x = 0.05$ can be associated to the presence of Co^{3+}, while the increase for the samples with $x \leq 0.03$ might be due to the increase of Co^{2+} ions.

Figure 12 shows M-$\chi_p$vs H curves for $Zn_{1-x}Co_xO$ ($0.0 \leq x \leq 0.08$) samples annealed for 3 h. The upper inset shows the variation of M_s and H_c with nominal Co doping. It can be seen that with increasing annealing time M_s decreased for $x = 0.01$, 0.03 and 0.05. Now, for $x = 0.08$ it was observed an increment in the FM behavior and for $x = 0.10$ the same SPM like behavior was observed but with lower M_s (see lower inset in Figure 12). According to these results, it is clear that the increment of annealing time decreases the FM behavior for $Zn_{1-x}Co_xO$ ($0.0 < x < 0.05$).

4. DISCUSSION

In brief, we will summarize the analysis of the different data collected using the various techniques. Undoped and Co doped ZnO samples with $x \leq 0.05$, annealed for 1 h and 3 h are pure and free of spurious phases. $ZnCo_2O_4$ was the only impurity phase identified in all the Co doped ZnO samples with $x \geq 0.08$. According to the results, we can divide $Zn_{1-x}Co_xO$ samples into 3 different groups. The first group with $x < 0.05$ can be considered as true solid solutions with only Co^{2+} ions into ZnO structure, the second group with $x = 0.05$, where there is a presence of multivalence Co ions, *i.e.* Co^{2+} and Co^{3+} without the formation

of an impurity phase, and finally the third group with $x > 0.05$ where there is a coexistence of $Zn_{1-x}Co_xO$ and of an impurity phase, more probably $ZnCo_2O_4$. In all samples there are isolated Co^{2+} ions that do not interact magnetically at RT, bringing about the observed PM signal, which increases with increasing Co concentration. *M* vs *T* curves suggest that some of these disordered Co^{2+} ions in $Zn_{1-x}Co_xO$ are AFM coupled. On the other hand, clearly the sharp reduction in the coercive field of $Zn_{1-x}Co_xO$ with ≥ 0.08 is due to the formation of $ZnCo_2O_4$. The magnetic signals in impurity-free samples are expected to be due to the random distribution of the Co ions, which results in the formation of isolated, pairs and very small clusters of Co ions at dopant concentrations below the percolation threshold. The RT PM behavior can easily be explained due to the presence of isolated ions, pairs, and magnetically coupled Co ions whose transition temperature are below RT. The AFM signal can be explained by the superexchange interactions between Co^{2+} ions.

Now, let us discuss the possible physical sources of the RTFM signal in our samples. The magnetic data revealed that M_S increases with increasing Co content and decreases with increasing annealing time. These results could indicate that percolation of bound magnetic polarons (BMPs) may be responsible for RTFM. Within the BMP model, the large density of oxygen vacancies and more concentration of dopants help to produce more BMPs, which yield a greater overall volume occupied by BMPs, leading to the overlap of BMPs and enhancing ferromagnetism, whereas with increasing annealing time the number of V_O decreases, therefore reducing the FM interaction. In order to predict if BMP model is suitable to explain the magnetic properties of $Zn_{1-x}Co_xO$ samples with $0.0.1 \leq x \leq 0.03$, we fitted the *M* vs *H* to the following equation:[50]

$$M = M_0 L(x) + \chi_p H$$

where the first term accounts for the BMP contribution and the second term is due to the observed PM contribution at higher field. Here, the spontaneous moment of the system is given by $M_0 = N m_s$, where N is the number of BMPs involved and m_s is the spontaneous magnetic moment per BMP. $L(x) = \coth(x) - \left(\frac{1}{x}\right)$ is the Langevin function with $x = \frac{m_{eff} H}{K_B T}$, where m_{eff} is the true spontaneous moment per BMP. At high temperature, the interaction between the BMPs can be ignored and $m_s = m_{eff}$. From Figure 13 it is observed that the Equation fits well the experimental data. The fitting parameters of the two curves are summarized in Table 1. From this table is noted that M_o and χ_p match well with data showed in Figures 9 and 11 (b) evidencing the goodness of fit. *N* values which were obtained from M_0 and m_{eff} are around $10^{13}/cm^3$, which is very small in comparison to required concentration of BPMs (~$10^{20}/cm^3$) for percolation in ZnO. [50] Additionally, is observed that this value decrease slightly with increasing Co concentration. Thus, the BPMs model is insufficient or not appropriated to explain RTFM in these Co doped ZnO samples. Thus, BPMs model does not seem to explain this behavior, then, it is necessary search for other type of models more commensurate with our results.

Now, it was observed that in $Zn_{1-x}Co_xO$ sample with $x = 0.05$, there was a mixed valence of Co ions (Co^{2+} and Co^{3+}) without the presence of impurity phase and a reduction of the M_s. The charge transfer ferromagnetic model, proposed by Coey *et al.* [51], [52] is based in the ability of the doped TM ions to exhibit mixed valence and exchange coupling to provide

electrons locally into the conduction band or to accept electrons from it. This model requires the existence of a defect-based band having a peak in the density of states (DOS) close to the Fermi level, a charge reservoir for transferring electrons, and an effective exchange integral associated with the defect states. Although there is a charge reservoir for transferring electrons, this model seems not to influence considerably the FM properties of $Zn_{1-x}Co_xO$ nanoparticles. According to XPS results, the Co^{3+} ions formed are presumably located in both, surface and core interstitial sites decreasing the oxygen-deficient regions. Therefore, possible excess or remnant donor defects cannot contribute to the charge transfer process and only form isolated spin polarons and Stoner criterion $N(E_f) > \frac{1}{I}$ is not satisfied. The reduction in magnetization in $Zn_{1-x}Co_xO$ with x = 0.05 can be related to decrease in oxygen vacancies within matrix ZnO. The presence of Co^{2+} in ZnO produce free charge carriers as well as V_O centers. When x reaches 0.05, and Co^{3+} ions are formed, results in the annihilation of V_O, by reducing the free charge carrier density. Then we need to find other possible sources for the RTFM signal.

In our previous paper we discussed the physical origin of the FM signal in Fe-Co co doped ZnO samples.[19] In that work the integral intensity of the EPR signal corresponding to the Co^{2+} ions was adequately fitted using the Curie law. The results from these fits showed negative Curie-Weiss temperature values suggesting that some Co^{2+} ions were weakly FM coupled. Therefore, we could expect a similar trend in the present samples, because they were prepared in the same way. Moreover, Acosta-Humánez *et. al* [14], Mesaros *et al.* [47] and Raita *et al.* [47] also reported FM coupling of Co ions in Co-doped ZnO nanoparticles prepared by modified sol-gel methods using EPR.

On the other hand, Straumal *et al*. [53] have proposed that the main factor controlling the ferromagnetic behavior of Co-doped ZnO is the value of the specific grain boundary area (s_{GB}). According to the authors, the Co doped ZnO becomes ferromagnetic if s_{GB} is higher than a certain threshold value $s_{th} = 1.5 \times 10^6 m^2/m^3$. The s_{GB} value can be calculated by using the formula $s_{GB} = 1.65/D_v$, where D_v is the mean crystal size.[54] Our samples shows typical values of $s_{GB} = 3{,}7 \times 10^7 m^2/m^3$, which is much higher than s_{th}. Therefore, FM can also arise due to the grain boundary in doped nanoparticles. This model could also contribute to the RTFM signal in our samples. Finally, the formation of different types of intrinsic defects and the perturbation/alteration and/or changes in the electronic structure of ZnO due to the incorporation of the Co^{2+} ions can be additional sources of FM in these samples.

5. CONCLUSIONS

We investigated in detail the crystallographic, optical, electronic and magnetic properties of sol-gel synthesized undoped and Co doped ZnO nanopowders. Within the detection limit of the techniques we found that the samples with less than 8 at. % of Co content were free of spurious phases, suggesting that the solubility limit were below that value. For the impurity-free samples, the high spin Co^{2+} ions replaced the Zn^{2+} ions at the ZnO lattice and for 5 at. % Co additionally Co^{3+} ions were detected. For these samples, the bang gap, *L* and both lattice parameters decrease with increasing Co content, whereas the PM and AFM signals, the average crystallite size and, *R* increase. Interestingly, the variation of M_s shows a similar trend as the intensity of the EPR signal intensity of Co^{2+} at 5K, suggesting that

these ions directly contributed to the FM signal. BPM model is insufficient to explain the RTFM in these Co doped ZnO samples and the charge transfer ferromagnetic model seems not influence considerably the FM properties of $Zn_{1-x}Co_xO$ nanoparticles According to the results obtained in this paper, the FM behavior may be originated from a combination of several factors such as the presence of high spin Co^{2+} ions, the formation of defect levels (free delocalized charge of carriers holes or electrons) close to the valence band edge and grain boundaries effects.

ACKNOWLEDGMENTS

This study was supported in Colombia by CODI-University of Antioquia (Sustainability Program for the Solid State Group 2014-2015 and project IN645CE). Research at Boise State University was supported by NSF CBET 1134468, NSF EAGER DMR-1137419, and ARO W911NF-09-1-0051 grants.

AUTHOR INFORMATION

Corresponding Author

*jjbj08@gmail.com

Author Contributions

All authors have given approval to the final version of the manuscript.

NOTES

The authors declare no competing financial interest.

REFERENCES

[1] S. J. Pearton, D. P. Norton, K. Ip, Y. W. Heo, and T. Steiner, “Recent progress in processing and properties of ZnO,” *Prog. Mater. Sci.*, vol. 50, pp. 293–340, 2005.

[2] Ü. Özgür, D. Hofstetter, and H. Morkoc, "ZnO Devices and Applications : A Review of Current Status and Future Prospects," *Proc. IEEE 98.7*, pp. 1255–1268, 2010.

[3] R. Janisch, P. Gopal, and N. A. Spaldin, "Transition metal-doped TiO2 and ZnO—present status of the field," *J. Phys. Condens. Matter*, vol. 17, pp. R657–R689, 2005.

[4] H. Ohno, "Making nonmagnetic semiconductors ferromagnetic," *Science (80-.).*, vol. 281, pp. 951–955, 1998.

[5] E.-C. Lee and K. Chang, "Ferromagnetic versus antiferromagnetic interaction in Co-doped ZnO," *Phys. Rev. B*, vol. 69, p. 085205, 2004.

[6] N. A. Spaldin, "A search for ferromagnetism in transition-metal-doped piezoelectric ZnO," *Phys. Rev. B*, vol. 69, p. 125201, 2003.

[7] P. Gopal and N. A. Spaldin, "Magnetic interactions in transition-metal-doped ZnO: An ab initio study," *Phys. Rev. B*, vol. 74, p. 094418, 2006.

[8] K. R. Kittilstved and D. R. Gamelin, "Manipulating polar ferromagnetism in transition-metal-doped ZnO: Why manganese is different from cobalt (invited)," *J. Appl. Phys.*, vol. 99, p. 08M112, 2006.

[9] D. A. Schwartz, N. S. Norberg, Q. P. Nguyen, J. M. Parker, and D. R. Gamelin, "Magnetic quantum dots: synthesis, spectroscopy, and magnetism of Co2+ - and Ni2+-doped ZnO nanocrystals.," *J. Am. Chem. Soc.*, vol. 125, pp. 13205–18, Oct. 2003.

[10] G. Lawes, A. S. Risbud, A. P. Ramirez, and R. Seshadri, "Absence of ferromagnetism in Co and Mn substituted polycrystalline ZnO," *Phys. Rev. B*, vol. 71, no. 4, p. 045201, 2005.

[11] A. Mesaros, C. D. Ghitulica, M. Popa, R. Mereu, A. Popa, T. Petrisor, M. Gabor, A. I. Cadis, and B. S. Vasile, "Synthesis, structural and morphological characteristics, magnetic and optical properties of Co doped ZnO nanoparticles," *Ceram. Int.*, vol. 40, pp. 2835–2846, 2014.

[12] J. Fu, X. Ren, S. Yan, Y. Gong, Y. Tan, K. Liang, R. Du, X. Xing, G. Mo, Z. Chen, Q. Cai, D. Sun, and Z. Wu, "Synthesis and structural characterization of ZnO doped with Co," *J. Alloys Compd.*, vol. 558, pp. 212–221, 2013.

[13] V. Gandhi, R. Ganesan, H. H. Abdulrahman Syedahamed, and M. Thaiyan, "Effect of Cobalt Doping on Structural, Optical, and Magnetic Properties of ZnO Nanoparticles Synthesized by Coprecipitation Method," *J. Phys. Chem. C*, vol. 118, pp. 9715–9725, 2014.

[14] F. Acosta-Humánez, R. Cogollo Pitalúa, and O. Almanza, “Electron paramagnetic resonance in Zn1-xCoxO,” *J. Magn. Magn. Mater.*, vol. 329, pp. 39–42, 2013.

[15] J. Hays, K. M. Reddy, N. Y. Graces, M. H. Engelhard, V. Shutthanandan, M. Luo, C. Xu, N. C. Giles, C. Wang, S. Thevuthasan, and A. Punnoose, “Effect of Co doping on the structural, optical and magnetic properties of ZnO nanoparticles.,” *J. Phys. Condens. Matter*, vol. 19, p. 266203, 2007.

[16] S. Kumar, S. Basu, B. Rana, A. Barman, S. Chatterjee, S. N. Jha, D. Bhattacharyya, N. K. Sahoo, and A. K. Ghosh, “Structural, optical and magnetic properties of sol–gel derived ZnO:Co diluted magnetic semiconductor nanocrystals: an EXAFS study,” *J. Mater. Chem. C*, vol. 2, pp. 481–495, 2014.

[17] N. Tahir, A. Karim, K. A. Persson, S. T. Hussain, A. G. Cruz, M. Usman, M. Naeem, R. Qiao, W. Yang, Y. Chuang, and Z. Hussain, “Surface Defects: Possible Source of Room Temperature Ferromagnetism in Co-Doped ZnO Nanorods,” *J. Phys. Chem. C*, vol. 117, pp. 8968–8973, 2013.

[18] “Pechini M.P. (1967) US Patent 3,330,697, 11 July 1967.”

[19] J. J. Beltrán, C. A. Barrero, and A. Punnoose, “Evidence of Ferromagnetic Signal Enhancement in Fe and Co Codoped ZnO Nanoparticles by Increasing Super fi cial Co 3 + Content,” *J. Phys. Chem. C*, vol. 118, pp. 13203–13217, 2014.

[20] J. J. Beltra, C. A. Barrero, and A. Punnoose, “Understanding the role of iron in the magnetism of Fe doped ZnO nanoparticles,” pp. 15284–15296, 2015.

[21] J. Li, L. Zhang, J. Zhu, Y. Liu, W. Hao, and B. Li, “Controllable synthesis and magnetic investigation of ZnO: Co nanowires and nanotubes,” *Mater. Lett.*, vol. 87, pp. 101–104, Nov. 2012.

[22] M. Li, J. Xu, X. Chen, X. Zhang, Y. Wu, P. Li, X. Niu, C. Luo, and L. Li, “Structural and optical properties of cobalt doped ZnO nanocrystals,” *Superlattices Microstruct.*, vol. 52, pp. 824–833, 2012.

[23] S. Shi, Y. Yang, J. Xu, L. Li, X. Zhang, G.-H. Hu, and Z.-M. Dang, “Structural, optical and magnetic properties of Co-doped ZnO nanorods prepared by hydrothermal method,” *J. Alloys Compd.*, vol. 576, pp. 59–65, Nov. 2013.

[24] H. Morkoç and Ü. Özgür, “General Properties of ZnO,” in *Zinc Oxide*, Wiley-VCH Verlag GmbH & Co. KGaA, 2009, pp. 1–76.

[25] N. M. Basith, J. J. Vijaya, L. J. Kennedy, M. Bououdina, S. Jenefar, and V. Kaviyarasan, “Co-Doped ZnO Nanoparticles: Structural, Morphological, Optical, Magnetic and Antibacterial Studies,” *J. Mater. Sci. Technol.*, vol. 30, pp. 1108–1117, 2014.

[26] M. Gaudon, O. Toulemonde, and A. Demourgues, “Green coloration of Co-doped ZnO explained from structural refinement and bond considerations.,” *Inorg. Chem.*, vol. 46, pp. 10996–1002, 2007.

[27] G. K. Williamson and W. H. Hall, “X-Ray Line Broadening From Filed Aluminium and Wolfram,” *Acta Metall.*, vol. 1, pp. 22–31, 1953.

[28] S. Kumar, S. Mukherjee, R. Kr. Singh, S. Chatterjee, and a. K. Ghosh, “Structural and optical properties of sol-gel derived nanocrystalline Fe-doped ZnO,” *J. Appl. Phys.*, vol. 110, p. 103508, 2011.

[29] A. Punnoose, K. Dodge, J. W. Rasmussen, J. Chess, D. Wingett, and C. Anders, “Cytotoxicity of ZnO Nanoparticles Can Be Tailored by Modifying Their Surface Structure: A Green Chemistry Approach for Safer Nanomaterials.,” *ACS Sustain. Chem. Eng.*, vol. 2, pp. 1666–1673, 2014.

[30] D. Stoltz, P. Palmgren, S. Yu, M. Go, and U. O. Karlsson, “Water Adsorption on ZnO (0001): Transition from Triangular Surface Structures to a Disordered Hydroxyl Terminated phase,” *J. Phys. Chem. C*, vol. 114, pp. 11157–11161, 2010.

[31] R. Elilarassi and G. Chandrasekaran, “Influence of Co-doping on the structural, optical and magnetic properties of ZnO nanoparticles synthesized using auto-combustion method,” *J. Mater. Sci. Mater. Electron.*, vol. 24, pp. 96–105, 2012.

[32] P. Koidl, “Optical absorption of Co2+ in ZnO,” *Phys. Rev. B*, vol. 15, pp. 2493–2499, 1977.

[33] M. K. Patra, K. Manzoor, M. Manoth, S. R. Vadera, and N. Kumar, “Studies on structural and magnetic properties of Co-doped pyramidal ZnO nanorods synthesized by solution growth technique,” *J. Phys. Chem. Solids*, vol. 70, no. 3–4, pp. 659–664, Mar. 2009.

[34] A. Escobedo, E. Sánchez, and U. Pal, “Use of diffuse reflectance spectroscopy for optical characterization of un-supported nanostructures,” *Rev. Mex. Física*, vol. 53, no. 5, pp. 18–22, 2007.

[35] M. Y. Nassar and I. S. Ahmed, “Hydrothermal synthesis of cobalt carbonates using different counter ions: An efficient precursor to nano-sized cobalt oxide (Co3O4),” *Polyhedron*, vol. 30, pp. 2431–2437, 2011.

[36] X. Qiu, L. Li, and G. Li, “Nature of the abnormal band gap narrowing in highly crystalline Zn[sub 1−x]Co[sub x]O nanorods,” *Appl. Phys. Lett.*, vol. 88, p. 114103, 2006.

[37] K. J. Kim and Y. R. Park, “Spectroscopic ellipsometry study of optical transitions in Zn[sub 1−x]Co[sub x]O alloys,” *Appl. Phys. Lett.*, vol. 81, p. 1420, 2002.

[38] X. Xu and C. Cao, “Hydrothermal synthesis of Co-doped ZnO flakes with room temperature ferromagnetism,” *J. Alloys Compd.*, vol. 501, pp. 265–268, 2010.

[39] J. Moulder and J. Chastain, “Handbook of X-ray Photoelectron Spectroscopy: ‘A Reference Book of Standard Spectra for Identification and Interpretation of XPS Data.’” Physical Electronics, 1995.

[40] T. Szörényi, L. D. Laude, I. Bertóti, Z. Kántor, and Z. Geretovszky, “Excimer laser processing of indium-tin-oxide films: An optical investigation,” *J. Appl. Phys.*, vol. 78, p. 6211, 1995.

[41] S. Bian, I. A. Mudunkotuwa, T. Rupasinghe, and V. H. Grassian, “Aggregation and Dissolution of 4 nm ZnO Nanoparticles in Aqueous Environments : Influence of pH , Ionic Strength , Size , and Adsorption of Humic Acid,” *Langmuir*, vol. 27, pp. 6059–6068, 2011.

[42] X. Bie, C. Wang, H. Ehrenberg, Y. Wei, G. Chen, X. Meng, G. Zou, and F. Du, “Room-temperature ferromagnetism in pure ZnO nanoflowers,” *Solid State Sci.*, vol. 12, pp. 1364–1367, 2010.

[43] L. Fu, Z. Liu, Y. Liu, B. Han, P. Hu, L. Cao, and D. Zhu, “Beaded Cobalt Oxide Nanoparticles along Carbon Nanotubes: Towards More Highly Integrated Electronic Devices,” *Adv. Mater.*, vol. 17, pp. 217–221, 2005.

[44] A. A. Khassin, T. M. Yurieva, V. V Kaichev, V. I. Bukhtiyarov, A. A. Budneva, E. A. Paukshtis, and V. N. Parmon, “Metal – support interactions in cobalt-aluminum co-precipitated catalysts : XPS and CO adsorption studies,” *J. Mol. Catal. A Chem.*, vol. 175, pp. 189–204, 2001.

[45] X. Wang, R. Zheng, Z. Liu, H.-P. Ho, J. Xu, and S. P. Ringer, “Structural, optical and magnetic properties of Co-doped ZnO nanorods with hidden secondary phases.,” *Nanotechnology*, vol. 19, p. 455702, 2008.

[46] J. F. Marco, J. R. Gancedo, J. Ortiz, and J. L. Gautier, “Characterization of the spinel-related oxides NixCo3−xO4 (x=0.3,1.3,1.8) prepared by spray pyrolysis at 350 °C,” *Appl. Surf. Sci.*, vol. 227, pp. 175–186, 2004.

[47] O. Raita, A. Popa, D. Toloman, M. Stan, A. Darabont, and L. Giurgiu, “Co2+ Ions in ZnO powders as seen by Magnetic Resonance,” *Appl. Magn. Reson.*, vol. 40, no. 2, pp. 245–250, 2011.

[48] P. Jakes and E. Erdem, “Finite size effects in ZnO nanoparticles: An electron paramagnetic resonance (EPR) analysis,” *Phys. status solidi*, vol. 5, pp. 56–58, 2011.

[49] S. K. S. Parashar, B. S. Murty, S. Repp, S. Weber, and E. Erdem, "Investigation of intrinsic defects in core-shell structured ZnO nanocrystals," *J. Appl. Phys.*, vol. 111, p. 113712, 2012.

[50] B. Pal and P. K. Giri, "High temperature ferromagnetism and optical properties of Co doped ZnO nanoparticles," *J. Appl. Phys.*, vol. 108, p. 084322, 2010.

[51] J. M. D. Coey, K. Wongsaprom, J. Alaria, and M. Venkatesan, "Charge-transfer ferromagnetism in oxide nanoparticles," *J. Phys. D. Appl. Phys.*, vol. 41, p. 134012, 2008.

[52] J. M. D. Coey, P. Stamenov, R. D. Gunning, M. Venkatesan, and K. Paul, "Ferromagnetism in defect-ridden oxides and related materials," *New J. Phys.*, vol. 12, p. 053025, 2010.

[53] B. B. Straumal, A. a. Mazilkin, S. G. Protasova, P. B. Straumal, A. a. Myatiev, G. Schütz, E. J. Goering, T. Tietze, and B. Baretzky, "Grain boundaries as the controlling factor for the ferromagnetic behaviour of Co-doped ZnO," *Philos. Mag.*, pp. 1–13, 2012.

[54] B. B. Straumal, A. a. Mazilkin, S. G. Protasova, A. a. Myatiev, P. B. Straumal, G. Schütz, P. a. Van Aken, E. Goering, and B. Baretzky, "Magnetization study of nanograined pure and Mn-doped ZnO films: Formation of a ferromagnetic grain-boundary foam," *Phys. Rev. B - Condens. Matter Mater. Phys.*, vol. 79, p. 205206, 2009.

TABLES

Table 1: Fitting parameters extracted from the BMP model.

$Zn_{1-x}Co_xO$	M_o (emu/g)	m_{eff} (emu)	χ_p (emu/gOe)	N^* cm^3
x=0.01	1.50×10^{-3}	2.61×10^{-16}	5.8×10^{-7}	3.25×10^{13}
x=0.03	1.70×10^{-3}	2.97×10^{-16}	2.58×10^{-6}	3.23×10^{13}

* Calculated data with the density obtained from XRD analysis.

FIGURE CAPTIONS

Figure 1: Rietveld refinement analysis of XRD patterns of Co doped ZnO samples annealed at 550 ºC for 1 h. Solid spheres are experimental data, whereas red solid lines represent the fit. The blue lines below represent the difference pattern. The top panel at the right side shows some selected expanded regions in the 31º to 37º 2θ range.

Figure 2: Variation of **(a)** *a* and *c* lattice parameters, **(b)** Zn–O bond length (*L*) parallel to the *c*-axis and average crystallite size (*Dv*), and **(c)** lattice distortion degree (*R*) and *c/a* ratio as a function ofCo content for all Co doped ZnO samples annealed for 1 h (left part) and for 3 h (right part).

Figure 3: FTIR spectra of $Zn_{1-x}Co_xO$ ($0 \leq x \leq 0.05$) samples annealed at 550 º C for 1 h.

Figure 4: (a) Optical absorbance spectra of ZnO and Co doped ZnO samples annealed at 550 º C for 1 h. The inset shows the variation of the observed (red solid spheres) and calculated [36] band gaps (blue solid triangles; see text) with the nominal Co content. **(b**) Derivative of absorbance spectra with respect to wavelength for $Zn_{1-x}Co_xO$ samples annealed at 550 ºC for 1 h.

Figure 5: (a) Optical absorbance spectra of ZnO and Co doped ZnO samples annealed at 550 º C for 3 h. The inset shows the variation of the observed (red solid spheres) and calculated [36] band gaps (blue solid triangles; see text) with the nominal Co content. **(b**) Derivative of absorbance spectra with respect to wavelength for $Zn_{1-x}Co_xO$ samples annealed at 550 ºC for 3 h.

Figure 6: (a) Wide survey X- ray photoelectron spectra of undoped ZnO and $Zn_{1x}Co_xO$ samples with $0.01 < x < 0.05$ samples annealed for 1h. The spectra of the core-electron regions of **(b)** Zn 2*p*, **(c)** O 1*s* and **(d)** Co 2*p* are also shown. The shadow areas in **(d)** represent the Co^{3+} component.

Figure 7: EPR spectra recorded at 5 K of Co doped ZnO samples annealed at 550 °C for 1 h. Inset **(a)** shows expanded region for $Zn_{0.99}Co_{0.01}O$ sample evidencing hyperfine splitting pointed out by arrows. Inset **(b)** shows the integrated intensity of the EPR spectra plotted as a function of *x*.

Figure 8: RT hysteresis loops for Co doped ZnO nanoparticles along with Co_3O_4 sample annealed for 1 h. The insets show hysteresis loops at 5 K.

Figure 9: RT magnetic hysteresis loops (M-$\chi_p$vs H) of $Zn_{1-x}Co_xO$ samples in the range of $0.0 \leq x \leq 0.08$ annealed for 1h. Lower inset shows M-$\chi_p$vs H for $Zn_{0.90}Co_{0.1}O$, while upper inset shows the variations of coercive field (H_c) and saturation magnetization (M_s) with nominal Co concentration. The dashed line in upper inset represents the M_s value of undoped ZnO.

Figure 10: $M(T)$ curves with H = 500 Oe for 1, 3, 5, 8 and 10 % Co doped ZnO samples annealead for 1h. The symbols (solid lines) correspond to ZFC (FC) data. The inset shows ZFC and FC curves for Co_3O_4.

Figure 11: Changes in **(a)** Curie constant (C) and Curie-Weiss temperature (θ) and **(b)** the linear paramagnetic component χ_p (obtained from Figure 8) and non-paramagnetic contributions, χ_o, of $Zn_{1-x}Co_xO$ samples as a function of x.

Figure 12: RT magnetic hysteresis loops (M-$\chi_p$vs H) of $Zn_{1-x}Co_xO$ samples with $0.0 \leq x \leq 0.08$ annealed for 3 h. Lower inset shows M-χ_p vs H for $Zn_{0.90}Co_{0.1}O$, while upper inset shows the variations of coercive field (H_c) and saturation magnetization (M_s) with nominal Co concentration.

Figure 13: Initial portion of the M vs H curve fitted with the BMP model [50] for $Zn_{1-x}Co_xO$ samples with $0.0.1 \leq x \leq 0.03$ annealed for 1h. Open symbols are experimental data and the solid lines represent the fit.

FIGURES

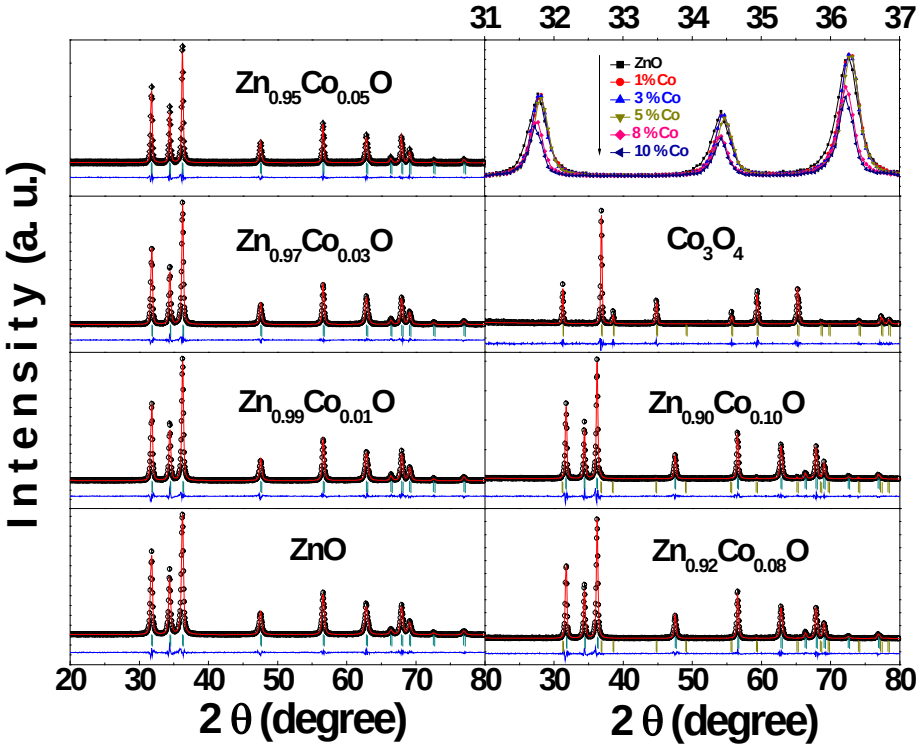

Figure 1: Rietveld refinement analysis of XRD patterns of Co doped ZnO samples annealed at 550 ºC for 1 h. Solid spheres are experimental data, whereas red solid lines represent the fit. The blue lines below represent the difference pattern. The top panel at the right side shows some selected expanded regions in the 31º to 37º 2θ range.

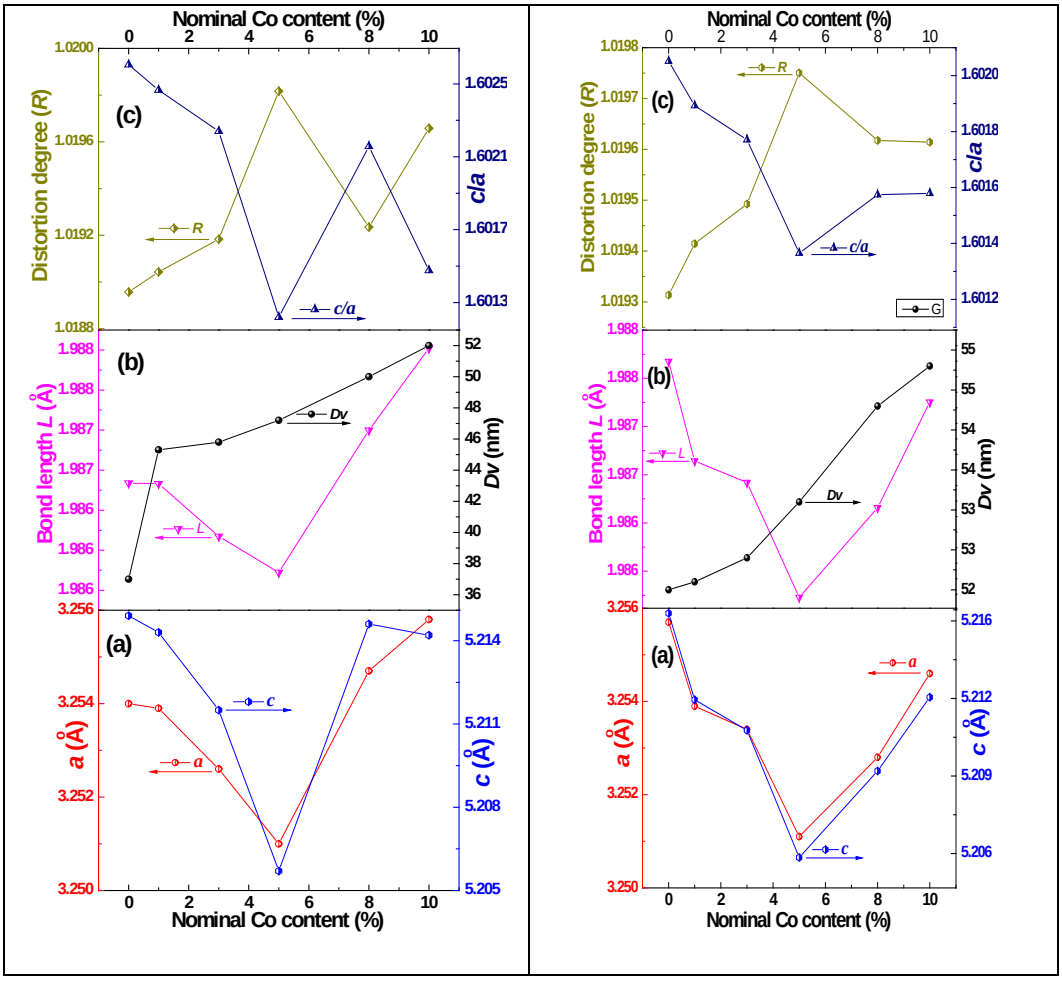

Figure 2: Variation of **(a)** *a* and *c* lattice parameters, **(b)** Zn–O bond length (*L*) parallel to the *c*-axis and average crystallite size (*Dv*), and **(c)** lattice distortion degree (*R*) and *c/a* ratio as a function ofCo content for all Co doped ZnO samples annealed for 1 h (left part) and for 3 h (right part).

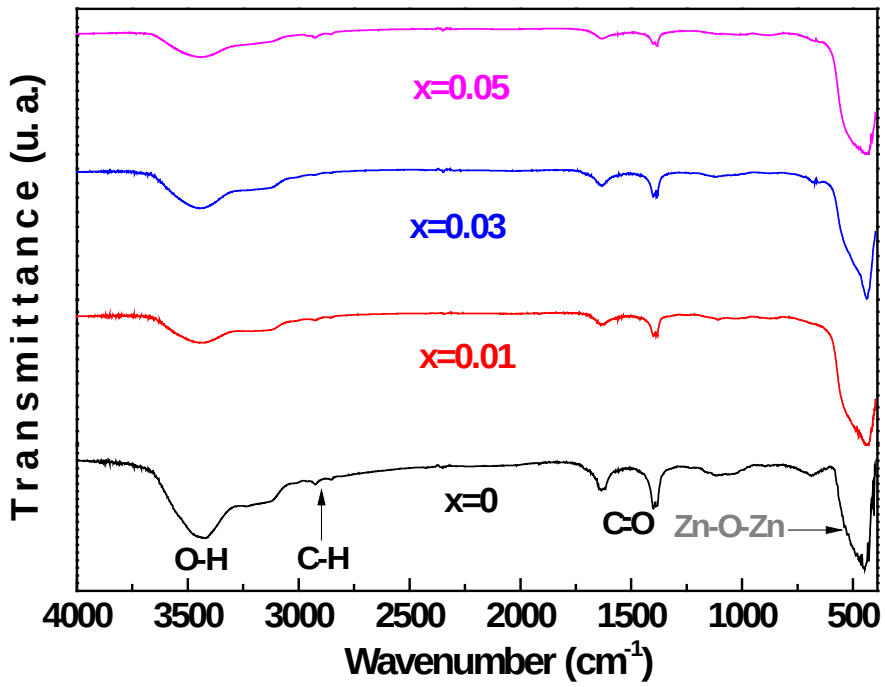

Figure 3: FTIR spectra of $Zn_{1-x}Co_xO$ ($0 \leq x \leq 0.05$) samples annealed at 550 ^{o}C for 1 h.

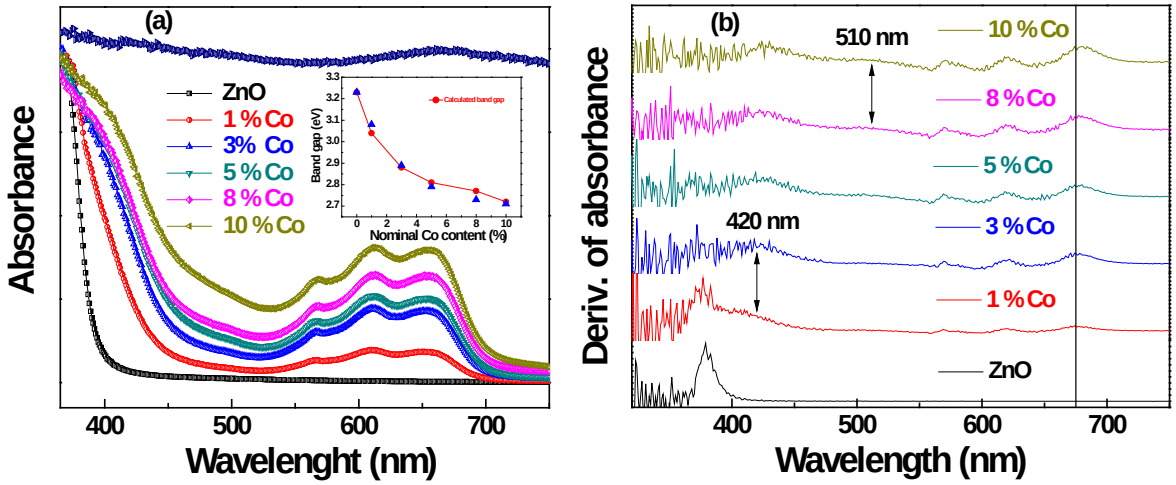

Figure 4: (a) Optical absorbance spectra of ZnO and Co doped ZnO samples annealed at 550 ^{o} C for 1 h. The inset shows the variation of the observed (red solid spheres) and calculated [36] band gaps (blue solid triangles; see text) with the nominal Co content. **(b)** Derivative of absorbance spectra with respect to wavelength for $Zn_{1-x}Co_xO$ samples annealed at 550 ^{o}C for 1 h.

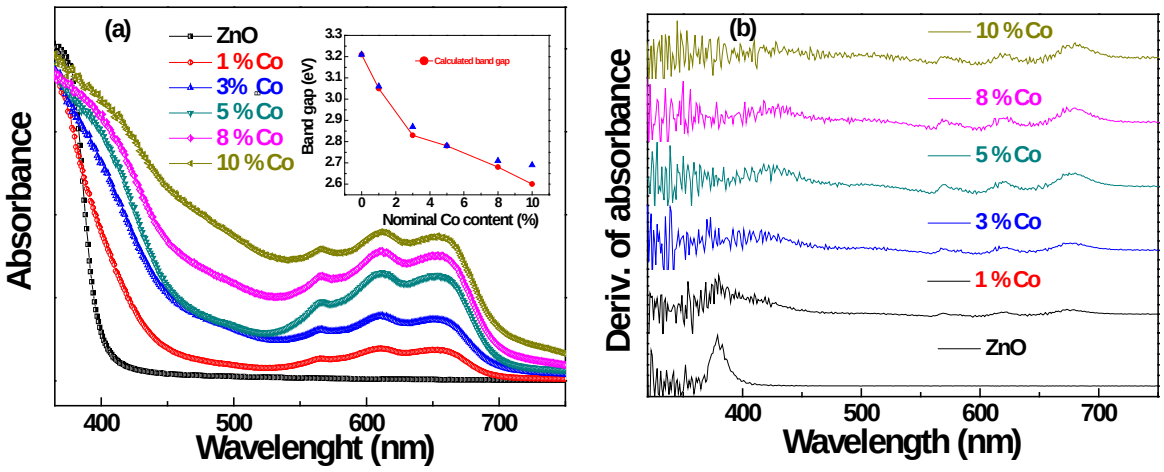

Figure 5: (a) Optical absorbance spectra of ZnO and Co doped ZnO samples annealed at 550 ^{o} C for 3 h. The inset shows the variation of the observed (red solid spheres) and calculated [36] band gaps (blue solid triangles; see text) with the nominal Co content. **(b)** Derivative of absorbance spectra with respect to wavelength for $Zn_{1-x}Co_xO$ samples annealed at 550 ^{o}C for 3 h.

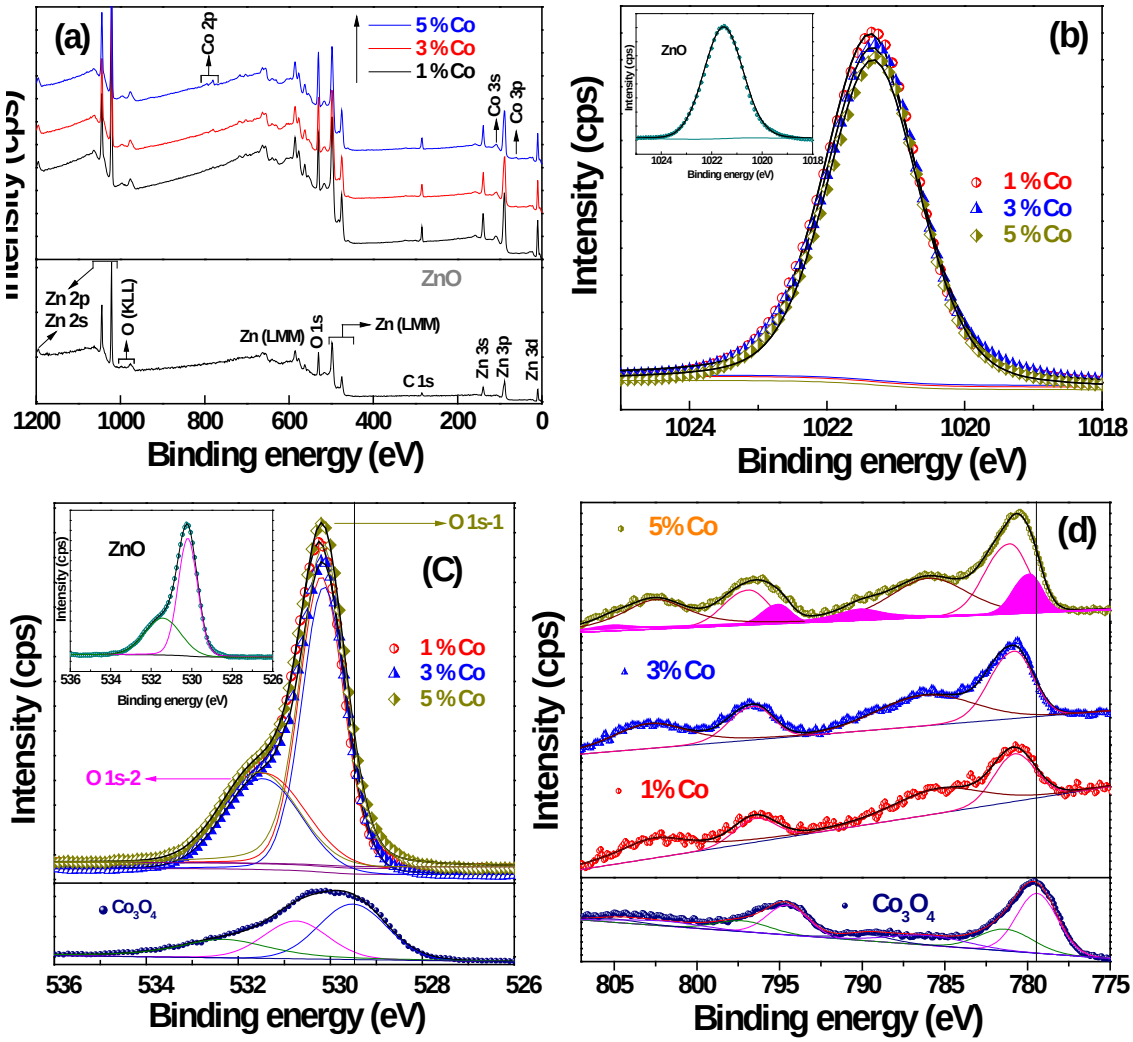

Figure 6: (a) Wide survey X- ray photoelectron spectra of undoped ZnO and $Zn_{1x}Co_xO$ samples with $0.01 < x < 0.05$ samples annealed for 1h. The spectra of the core-electron regions of **(b)** Zn 2*p*, **(c)** O 1*s* and **(d)** Co 2*p* are also shown. The shadow areas in **(d)** represent the Co^{3+} component.

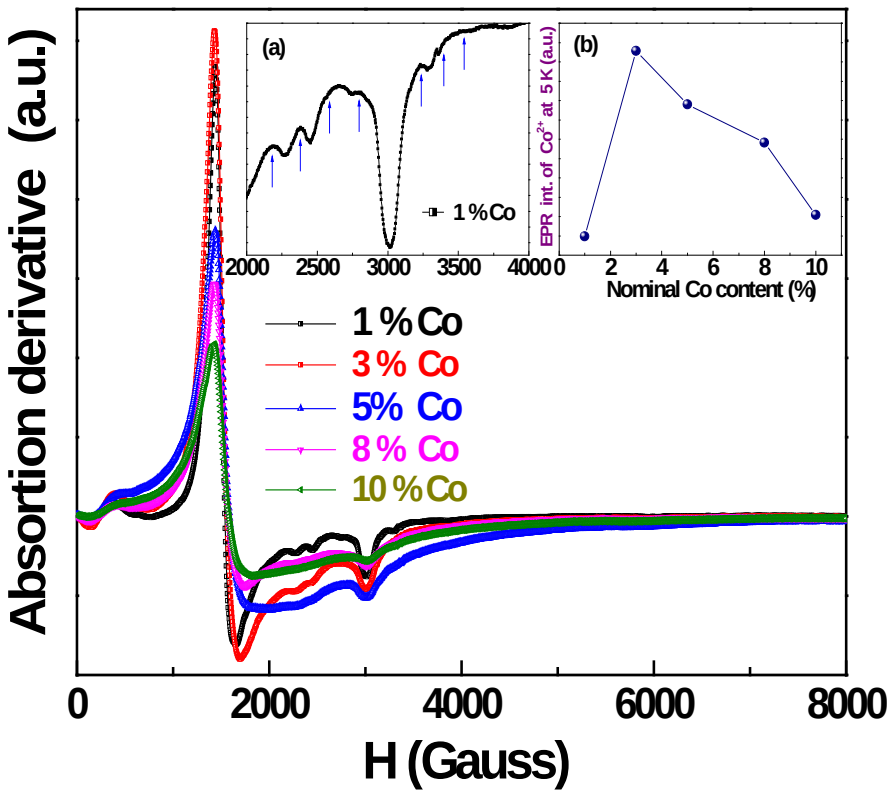

Figure 7: EPR spectra recorded at 5 K of Co doped ZnO samples annealed at 550 °C for 1 h. Inset **(a)** shows expanded region for $Zn_{0.99}Co_{0.01}O$ sample evidencing hyperfine splitting pointed out by arrows. Inset **(b)** shows the integrated intensity of the EPR spectra plotted as a function of *x*.

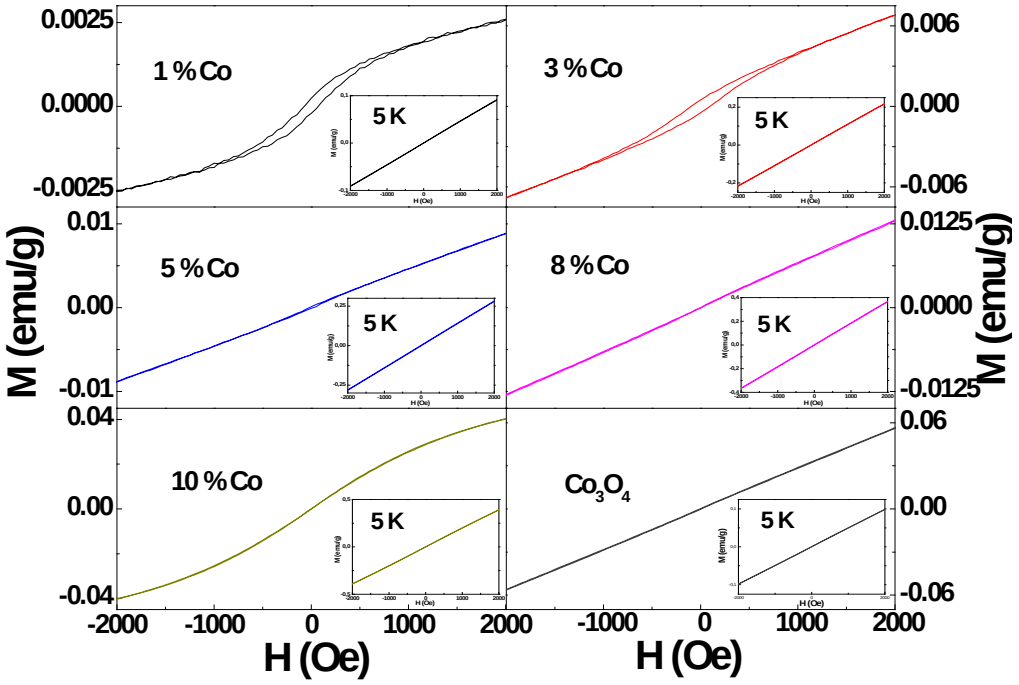

Figure 8: RT hysteresis loops for Co doped ZnO nanoparticles along with Co_3O_4 sample annealed for 1 h. The insets show hysteresis loops at 5 K.

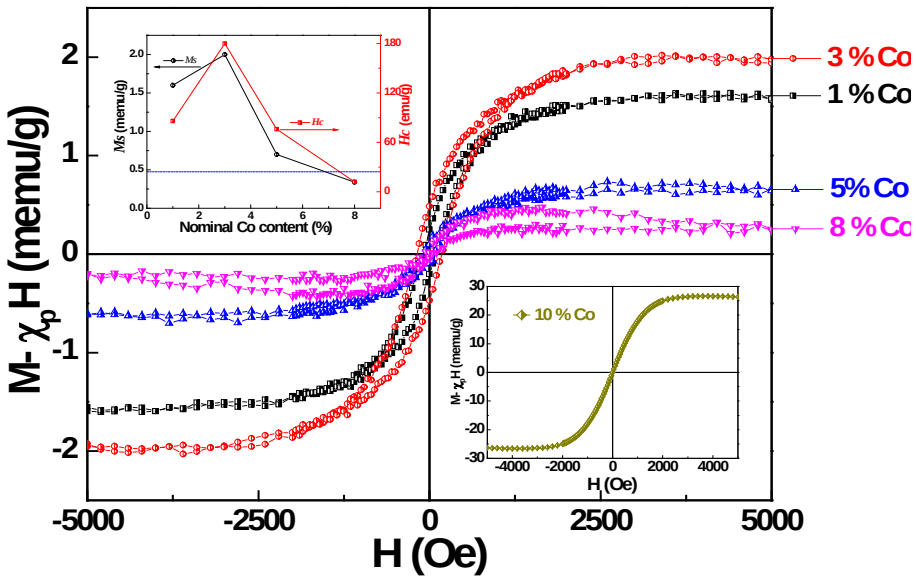

Figure 9: RT magnetic hysteresis loops (M-$\chi_p$vs H) of $Zn_{1-x}Co_xO$ samples in the range of $0.0 \leq x \leq 0.08$ annealed for 1h. Lower inset shows M-$\chi_p$vs H for $Zn_{0.90}Co_{0.1}O$, while upper inset shows the variations of coercive field (H_c) and saturation magnetization (M_s) with nominal Co concentration. The dashed line in upper inset represents the M_s value of undoped ZnO.

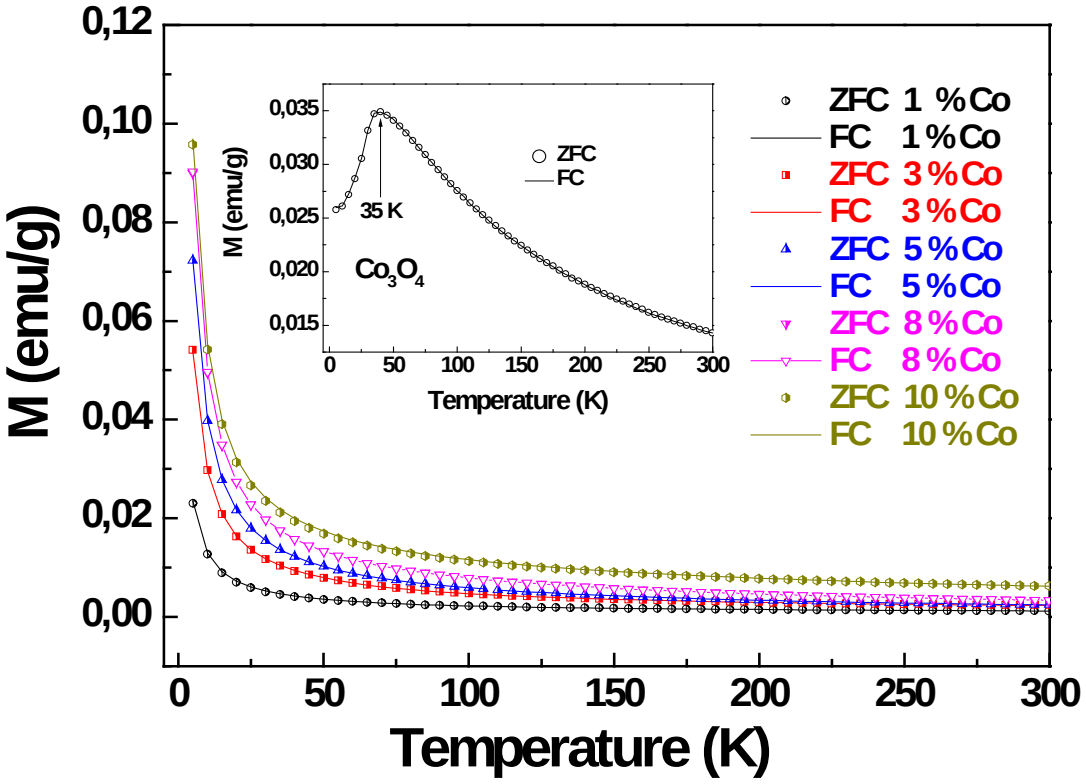

Figure 10: *M(T)* curves with H = 500 Oe for 1, 3, 5, 8 and 10 % Co doped ZnO samples annealead for 1h. The symbols (solid lines) correspond to ZFC (FC) data. The inset shows ZFC and FC curves for Co_3O_4.

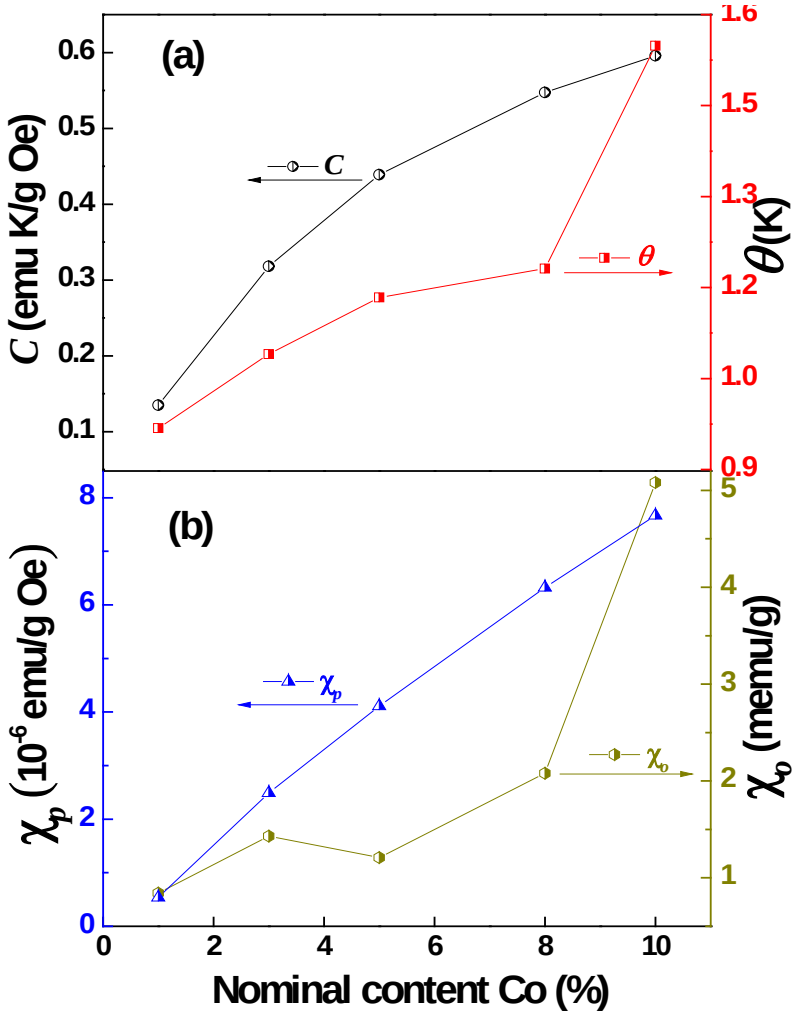

Figure 11: Changes in **(a)** Curie constant (C) and Curie-Weiss temperature (θ) and **(b)** the linear paramagnetic component χ_p (obtained from Figure 8) and non-paramagnetic contributions, χ_o, of $Zn_{1-x}Co_xO$ samples as a function of x.

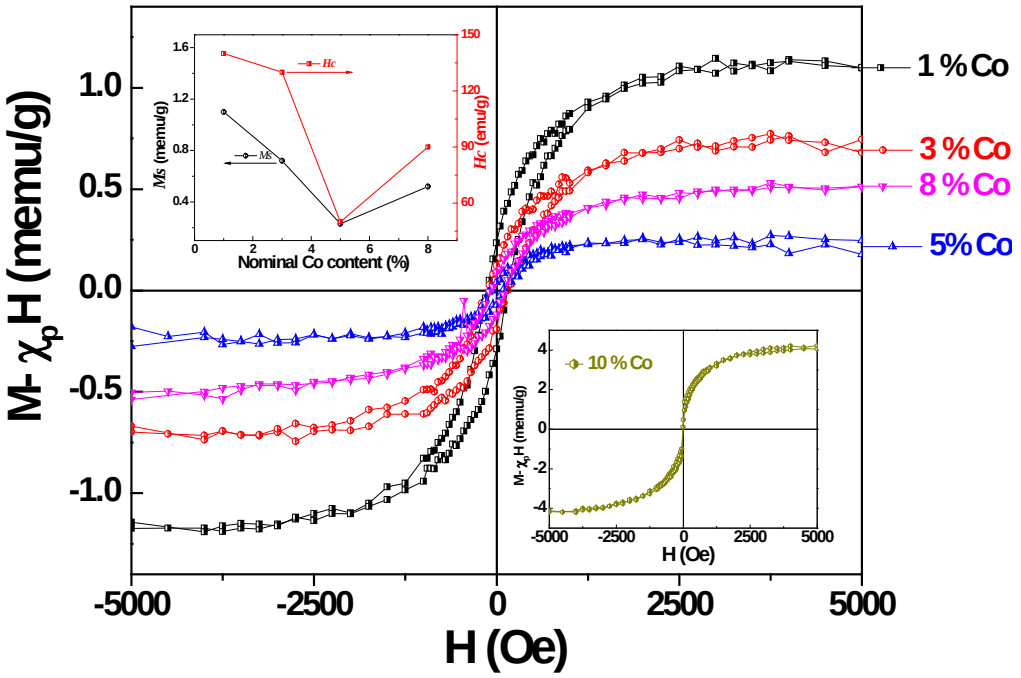

Figure 12: RT magnetic hysteresis loops (M-$\chi_p$vs H) of $Zn_{1-x}Co_xO$ samples with $0.0 \leq x \leq 0.08$ annealed for 3 h. Lower inset shows M-χ_p vs H for $Zn_{0.90}Co_{0.1}O$, while upper inset shows the variations of coercive field (H_c) and saturation magnetization (M_s) with nominal Co concentration.

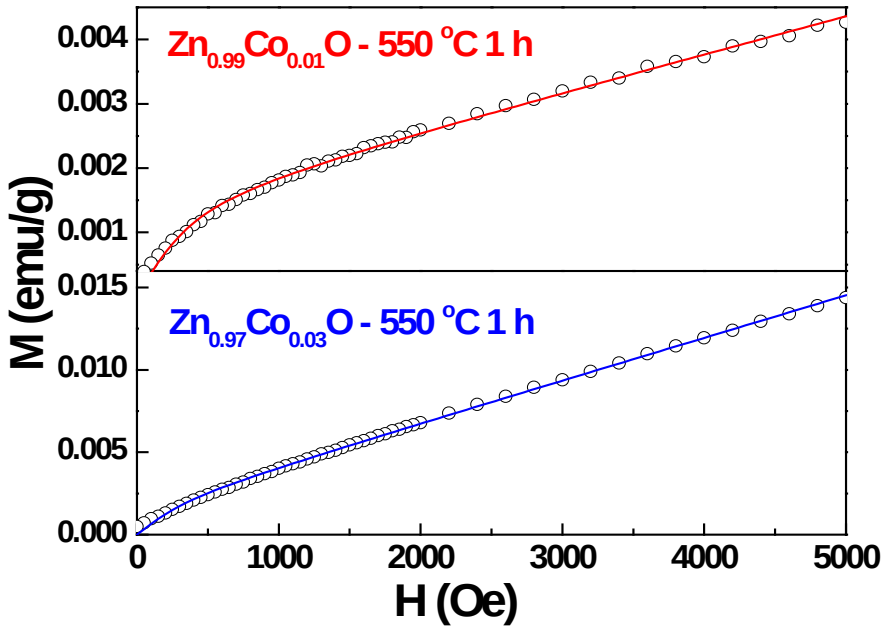

Figure 13: Initial portion of the *M* vs *H* curve fitted with the BMP model [50] for $Zn_{1-x}Co_xO$ samples with $0.0.1 \leq x \leq 0.03$ annealed for 1h. Open symbols are experimental data and the solid lines represent the fit.